

MonoGSDF: Exploring Monocular Geometric Cues for Gaussian Splatting-Guided Implicit Surface Reconstruction

Kunyi Li^{1,3 *} Michael Niemeyer² Zeyu Chen⁴ Nassir Navab^{1,3} Federico Tombari^{1,2}

¹Technical University of Munich ²Google ³Munich Center for Machine Learning ⁴Tsinghua University

Abstract

Accurate meshing from monocular images remains a key challenge in 3D vision. While state-of-the-art 3D Gaussian Splatting (3DGS) methods excel at synthesizing photorealistic novel views through rasterization-based rendering, their reliance on sparse, explicit primitives severely limits their ability to recover watertight and topologically consistent 3D surfaces. We introduce MonoGSDF, a novel method that couples Gaussian-based primitives with a neural Signed Distance Field (SDF) for high-quality reconstruction. During training, the SDF guides Gaussians' spatial distribution, while at inference, Gaussians serve as priors to reconstruct surfaces, eliminating the need for memory-intensive Marching Cubes. To handle arbitrary-scale scenes, we propose a scaling strategy for robust generalization. A multi-resolution training scheme further refines details and monocular geometric cues from off-the-shelf estimators enhance reconstruction quality. Experiments on real-world datasets show MonoGSDF outperforms prior methods while maintaining efficiency.

1. Introduction

3D Gaussian Splatting (3DGS) [16] has emerged as a state-of-the-art method for high-quality novel view synthesis by leveraging the rasterization pipeline and representing 3D scenes using points characterized by Gaussian functions. However, 3DGS remains an explicit and discrete representation, posing challenges for accurate 3D surface reconstruction and meshing. This limitation is particularly important for applications such as geometry editing [6, 36, 43], 3D animation [30, 33, 49], and robotics [15, 50, 56]. The primary challenge lies in 3DGS being a discrete and unstructured point-based geometry representation. Given that 3D Gaussians are primarily optimized for accurate appearance rendering rather than geometric regularization, which complicates the extraction of accurate 3D surfaces through post-processing methods like Poisson surface reconstruc-

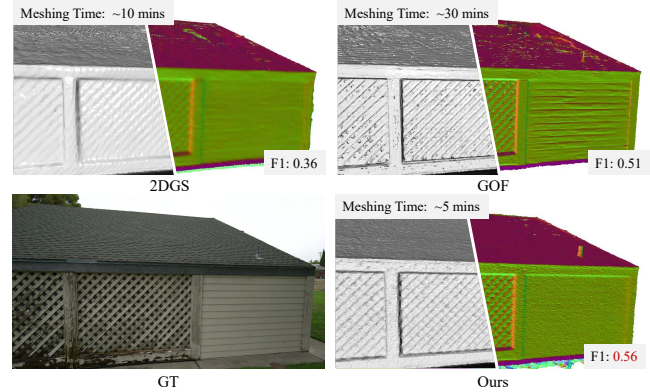


Figure 1. **MonoGSDF**. Ours achieves superior surface reconstruction on arbitrary-scale scenes, particularly in areas with limited view coverage. Compared to 2DGS [12] and GOF [48], ours achieves higher F1 scores (\uparrow) and reconstructs smooth surfaces with fine details.

tion [14].

These challenges have motivated recent investigations exploring how 3DGS can be used for high-quality surface reconstruction while maintaining its rendering speed and efficiency. Methods like 2DGS [12] address this by aligning 2D Gaussians to surfaces, although their depth map-based mesh extraction [7] struggles with thin structures and unbounded scenes due to resolution and resource limitations. Methods such as SuGaR [11] attempt to address these limitations by aligning 3D Gaussians with mesh faces, while DN-Splatler [34] incorporates depth and normal estimators. Nevertheless their reliance on Poisson reconstruction [14] still fundamentally limits reconstruction and meshing quality due to the inherent geometric inaccuracies of Gaussian representations. Although recent methods [24, 45, 55] have integrated SDF fields into Gaussian training for surface reconstruction, their incomplete exploration of the Gaussian-SDF relationship results in over-smoothed surfaces and limits their application within object-level reconstruction.

To bridge the gap between explicit Gaussian representations and implicit surface reconstruction while fully

*kunyi.li@tum.de

leveraging their complementary advantages, we present MonoGSDF, a unified framework that establishes a robust connection between 3D Gaussians and SDF-based surface modeling for high-fidelity reconstruction. Our **contributions** are:

- A Gaussian-based implicit surface reconstruction pipeline for monocular images, where the SDF guides Gaussians to better align near the surface during training, while Gaussians act as priors for fast zero-level set extraction during reconstruction.
- A simple yet efficient SDF-to-Opacity function that bridges implicit SDF with explicit Gaussians, coupled with a Gaussian-guided normalization strategy that dynamically maps unbounded 3D coordinates to a $(0,1)$ range with minimal distortion.
- A multi-resolution training strategy based on wavelet transforms progressively refines details, while off-the-shelf geometric cues further enhance reconstruction quality, enabling Gaussians to better capture scene geometry.

Experiments on real-world datasets demonstrate that our method delivers high-quality reconstructions and outperforms baselines by 13% in terms of Chamfer distance while preserving the view synthesis quality.

2. Related Works

2.1. View Synthesis and Gaussian Splatting

Neural Radiance Field (NeRF) [25] utilize multi-layer perceptions (MLP) as scene representation to predict geometry and view-dependent appearance. The MLP is optimized via a photometric loss through volume rendering. Subsequent methods have focused on optimizing NeRF’s training and expressiveness using grid representations [28], improving rendering speed [32, 53] and scaling to unbounded scenes [3]. However, volume rendering typically requires substantial computational resources and extensive training durations. 3D Gaussian Splatting (3DGS) [16] has emerged as an efficient approach for real-time view synthesis through differentiable Gaussian functions. Subsequent works have enhanced rendering quality via anti-aliasing techniques [31, 40, 47] and improved rendering speed through Gaussian density control [42] and radiance field priors [22, 29]. Geometry-focused approaches like DNGaussian [19] address sparse view degradation, while GeoGaussian [20] preserves non-textured regions. Instantsplat [9] accelerates sparse view training using Dust3r [38] initialization, and Scaffold-GS [23] combines implicit-explicit representations. However, these methods primarily focus on appearance quality rather than underlying geometry, limiting their application to view synthesis.

2.2. Surface Reconstruction from Gaussians

Due to the discrete and unstructured nature of 3DGS, along with supervision being limited to RGB images during training, existing methods often struggle to accurately capture scene geometry, making surface reconstruction particularly challenging. SuGaR [11] addresses this by constructing a density field from Gaussians and extracting meshes via level-set searching. However, it is computationally expensive and struggles to reconstruct large, smooth surfaces like floors and walls. Other approaches [4, 5, 34, 39, 51] incorporate depth or normal estimators as priors to supervise Gaussians. 2DGS [12] and GSurfels [8] improves geometric alignment by flattening 3D Gaussians into 2D disks or surfels, enabling better surface representation. For surface reconstruction, they rely on either multi-view depth maps for TSDF fusion or Poisson reconstruction. However, TSDF fusion is constrained by fixed resolution and high memory usage for large scenes. To handle unbounded scenes, it requires contracting coordinates, introducing unnecessary distortions. Meanwhile, Poisson reconstruction often produces noisy surfaces due to inaccuracies in Gaussian geometry distribution. Instead of refining depth and normal maps, some methods [2, 24, 45, 55] integrate Signed Distance Field (SDF). 3DGSR [24] and GSDF [45] associate Gaussians with SDF via an additional branch that volume-renders depth and normal supervised by rendered Gaussian depth and normal. However, this approach is inefficient and fails to fully exploit the relationship between Gaussians and SDF. GS-Pull [55] and GSurf [2] improve upon this by leveraging SDF gradients to better align Gaussians with surfaces, but they are either restricted to object-level reconstruction or produce overly smooth results. Gaussian Opacity Fields (GOF) [48] approximates minimum accumulated alpha values from all views via ray tracing to construct an opacity field, followed by surface extraction using Marching Tetrahedra [18]. However, Gaussian distributions remain inconsistent and unstructured relative to scene surfaces. Our method leverages SDF to guide Gaussians to align closer to the surface during training. At inference, Gaussians serve as primitives to efficiently constrain zero-level set extraction, avoiding redundant free-space searches while achieving accurate reconstruction.

3. Method

3.1. Preliminaries

3D Gaussian Splatting. 3D Gaussian Splatting (3DGS) [16] employs a set of 3D points to effectively render images from given viewpoints, each characterized by a Gaussian function with 3D mean $\mu_i \in \mathbb{R}^3$, covariance matrix $\Sigma_i \in \mathbb{R}^{3 \times 3}$, opacity value $\alpha_i \in \mathbb{R}$, RGB color values $\mathbf{c}_i \in \mathbb{R}^3$:

$$o_i(\mathbf{x}) = \alpha_i * \exp \left(-\frac{1}{2} (\mathbf{x} - \mu_i)^T \Sigma_i^{-1} (\mathbf{x} - \mu_i) \right). \quad (1)$$

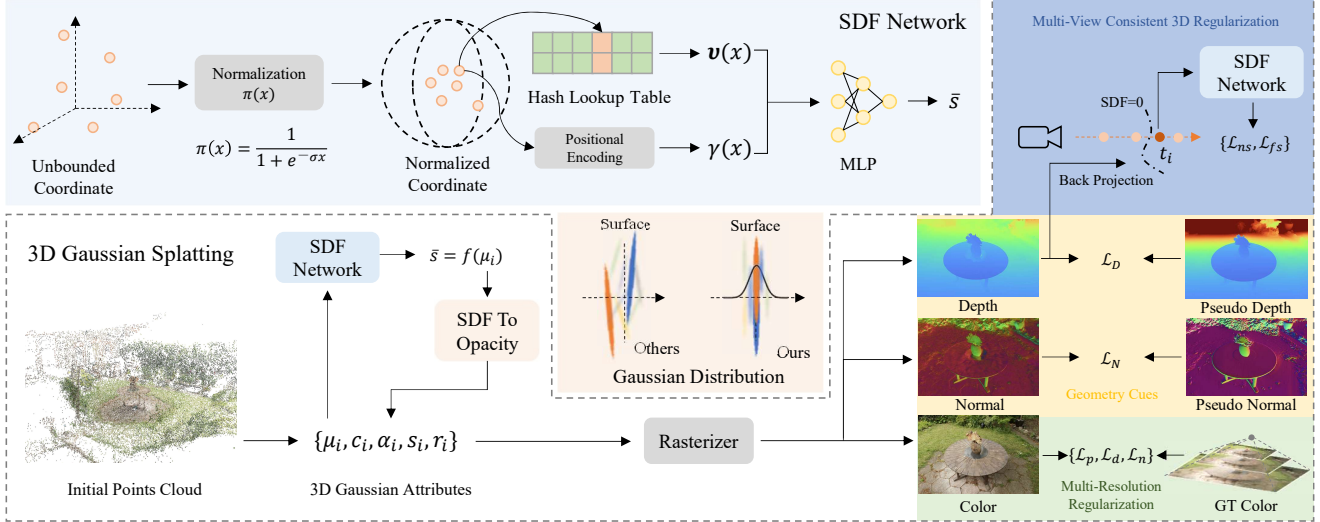


Figure 2. **Overview.** MonoGSDF establishes a synergistic relationship between SDF and Gaussian representation: the SDF regulates Gaussian distribution during training, while Gaussians serve as efficient primitives for rapid surface extraction. We first query the SDF values for each Gaussians and convert them into opacity values. This enforces Gaussian to stick closer to the surface. Then we follow the standard rasterization pipeline to render color, depth and normal maps. Off-the-shelf geometry cues and multi-resolution strategy are applied for better geometry performance. And we jointly train the SDF via 3D supervision signal from rendered Gaussian depth.

Given a 3D position \mathbf{x} , $o_i(\mathbf{x})$ represents current opacity value contributed by the i -th Gaussian. To facilitate optimization, Σ_i is factorized into the product of a scaling matrix S_i , represented by scale factors $\mathbf{s}_i \in \mathbb{R}^3$, and a rotation matrix R_i encoded by a quaternion $\mathbf{r}_i \in \mathbb{R}^4$:

$$\Sigma_i = R_i S_i S_i^T R_i^T. \quad (2)$$

3D Gaussians are then projected onto a 2D image plane according to elliptical weighted average (EWA) [57] to render images for given views. Color $\bar{\mathbf{C}}(\mathbf{u})$, depth $\bar{D}(\mathbf{u})$, and normal $\bar{\mathbf{N}}(\mathbf{u})$ at pixel \mathbf{u} is rendered by N projected and ordered Gaussians using point-based α -blending:

$$\{\bar{\mathbf{C}}, \bar{D}, \bar{\mathbf{N}}\}(\mathbf{u}) = \sum_{i \in N} T_i o_i \{\mathbf{c}_i, d_i, \mathbf{n}_i\}, \quad (3)$$

where $T_i = \prod_{j=1}^{i-1} (1 - o_j)$, depth d_i is the distance between camera center and the ray-Gaussian intersection plane, and Gaussian's normal \mathbf{n}_i is approximated as the normal of the ray-Gaussian intersection plane.

Neural Signed Distance Field. While 3DGS excels in novel view synthesis, its discrete nature limits surface reconstruction. In contrast, SDF provide a continuous, watertight surface as the zero-level set. We use a hash-based neural representation and jointly train the SDF with 3DGS, enabling more precise and efficient surface extraction. To better encode the scene geometry, we choose One-blob $\gamma(\mathbf{x})$ [26] as positional embedding and a multi-resolution hash-based feature grid $\mathcal{V} = \{\mathcal{V}^l\}_{l=1}^L$ [28]. Feature $\mathcal{V}(h(\mathbf{x}))$ at

any 3D point \mathbf{x} are queried via trilinear interpolation. The geometry decoder f is an MLP which maps the 3D coordinate to an SDF value \bar{s} :

$$f(\mathbf{x}) = f(\gamma(h(\mathbf{x})), \mathcal{V}(h(\mathbf{x}))) \mapsto \bar{s}. \quad (4)$$

where h is a coordinate normalization. Therefore, for each 3D Gaussian located at μ_i , its corresponding SDF value can be written as $\bar{s}_i = f(\mu_i)$.

3.2. Gaussian-Guided Signed Distance Field

Connect Gaussians with SDF. As illustrated in Figure 2, our method begins by querying SDF values with each Gaussian 3D mean μ_i using Eq. 4, where zero values correspond to surface points. While 3DGSR [24] introduced a bell-shaped function to map SDF value to Gaussian opacity, this approach assigns an opacity value $\alpha_i = 0.25$ to surface points ($\bar{s} = 0$), which contradicts the physical reality that surface points should exhibit maximum opacity ($\alpha_i = 1$). To address this limitation, we propose a Gaussian-shaped transformation that maintains both mathematical simplicity and computational efficiency while ensuring physically plausible opacity values $g(\bar{s})$:

$$g(\bar{s}_i) = \exp(-(\beta * \bar{s}_i)^2) \mapsto \alpha_i, \quad (5)$$

where β is a hyperparameter. While previous 3DGS methods [12, 16, 23] optimize opacities through alpha blending without considering spatial distribution constraints, these approaches often result in limited geometric accuracy. Our

method enforces a better distribution of Gaussians along the surface, leading to high geometric fidelity.

Gaussian-Guided Normalization Our rendering pipeline follows the standard Gaussian rasterization process, generating color \bar{C} , depth \bar{D} and \bar{N} maps from Gaussian attributes, with the depth map subsequently used for SDF training. While 3DGSR [24] and GSDF [45] have adopted similar approaches, their grid-based representations necessitate predefined scene bounding boxes for volume initialization, restricting their applicability to object-level or small-scale scene reconstruction. Although MipNeRF [3] introduced a fixed coordinate contraction method for unbounded scenes, its mapping of infinite space to $[-2, 2]$ conflicts with our hash-based feature field’s requirement for $(0, 1)$ input. Moreover, MipNeRF’s linear transformation within a limited region of interest introduces substantial distortion in peripheral areas. To address these limitations and to enable scalable reconstruction of real-world unbounded scenes, our method introduces a Gaussian-guided normalization strategy. We first establish a bounding box based on the Gaussians, then apply a novel sigmoid-like normalization function that maps 3D point $\mathbf{x} \in \mathbb{R}^3$ to a fixed $(0, 1)$ range:

$$h(\mathbf{x}) = 1/(1 + \exp(-\sigma\mathbf{x})), \quad (6)$$

where $\sigma = 2/B$, $B \in \mathbb{R}^3$ is the bounding box size of initial Gaussians. This approach ensures the volume containing the primary Gaussians occupies the majority of the grid space. During Gaussian densification, while new Gaussians may extend beyond the initial bounding box, they remain within the normalized scope. Our sigmoid-like normalization maintains near-linear transformation for Gaussians within the primary bounding box while effectively contracting distant Gaussians, achieving minimal distortion.

3.3. Optimization

Training our Gaussian-guided SDF presents unique challenges: enforcing all Gaussians to satisfy the condition $\bar{s}_i = 0$ degrades rendering quality by removing opacity variations, while sparse Gaussian-based SDF supervision lacks spatial coverage. Volume rendering methods like 3DGSR [24] introduce computational overhead and limited 2D supervision is insufficient for accurate 3D representation. Our solution introduces a novel framework that enhance the Gaussians with an off-the-shelf geometry estimator and supervise the SDF with a dense 3D regularization through depth back-projection.

Geometry Cues. To enhance reconstruction quality in real-world scenarios, we integrate an off-the-shelf monocular depth estimator* to obtain dense per-pixel disparity priors as \hat{Z} . However, these estimated pseudo disparity measurements exhibit significant scale ambiguity and suffer

*We use DepthAnything V2 [41] in this work.

from multi-view inconsistency. While DN Splatter [34] addresses this issue through direct depth alignment, applying a transformation $\bar{D} = s\hat{D} + t$, their method fails to account for shifts in disparity \hat{Z} , resulting in distance-dependent scale variations. To ensure robust relative scale consistency, we first utilize the rendered depth to correct the pseudo disparity and obtain the pseudo depth $\hat{D} = a/(s * \hat{Z} + t) + b$:

$$\mathcal{L}_D = \sum |(a/(s * \hat{Z} + t) + b - \bar{D})|. \quad (7)$$

where s, t and a, b represent learnable scale and shift parameters. We further convert the aligned depth into pseudo normal $\hat{N} = \nabla \hat{D} / \|\nabla \hat{D}\|$, providing a more stable supervision signal for Gaussian training:

$$\mathcal{L}_N = \sum (1 - \hat{N} \cdot \bar{N}). \quad (8)$$

where \bar{N} is rendered Gaussian normal. Therefore, the overall geometry regularization is $\mathcal{L}_{geo} = \lambda_D \mathcal{L}_D + \lambda_N \mathcal{L}_N$.

While the geometry cues offer valuable 2D supervision for improving depth and normal, they fail to constrain the 3D Gaussian distribution effectively. We address this limitation through the SDF, which enforces tied surface alignment of Gaussians.

Multi-View Consistent 3D Regularization. Directly supervising SDF with monocular geometry cues like MonoSDF [46] suffers from scale ambiguity and lacks multi-view consistency. Further, volume rendering-based supervision as proposed in 3DGSR [24] and GSDF [45] are inefficient and only supervise SDF with rendered Gaussian depth map in 2D. Our approach combines monocular cues with the inherent advantages of 3D Gaussians that the Gaussian-rendered depth \bar{D} naturally maintains multi-view consistency and enables reliable 3D signal supervision for SDF through back-projection.

More specifically, we first sample M pixels $\{\mathbf{u} = \mathbf{u}_i \mid \mathbf{u}_i \in \mathbb{R}^2, \text{ for } i = 1, 2, \dots, M\}$ from the rendered Gaussian depth map \bar{D} . For each ray casts from a pixel, we sample $K = K_n + K_f$ points $\{t_k\}$ from the camera center to the surface, where K_n means near surface samples and K_f means free space samples. SDF values of each point can be queried as $\{\bar{s}_k\}$. For near surface samples within the truncation region tr , i.e. $S_{tr} = \{|\bar{D}(\mathbf{u}) - t_k| \leq tr\}$, we use the distance between the sampled point t_k and its surface $\bar{D}(\mathbf{u}_j)$ as an approximation of ground truth SDF value for supervision:

$$\mathcal{L}_{ns} = \sum_{\mathbf{u}_j \in \mathbf{u}} \sum_{t_k \in S_{tr}} \|\bar{s}_k - (\bar{D}(\mathbf{u}_j) - t_k)\|_2. \quad (9)$$

For points that are far from the surface $S_{fs} = \{\bar{D}(\mathbf{u}) - t_k > tr\}$, we apply a free-space supervision as:

$$\mathcal{L}_{fs} = \sum_{\mathbf{u}_j \in \mathbf{u}} \sum_{t_k \in S_{fs}} \|\bar{s}_k - 1\|_2. \quad (10)$$

Therefore, the overall SDF regularization is $\mathcal{L}_{sdf} = \lambda_{ns}\mathcal{L}_{ns} + \lambda_{fs}\mathcal{L}_{fs}$.

Multi-Resolution Regularization. Unlike vanilla 3DGS [16] that uses L1 and SSIM losses with opacity-based pruning, our method links opacity to spatial position, lifting the need for *Opacity Resets* but potentially causing Gaussian redundancy. While low-to-high frequency strategies [52] can accelerate convergence, they risk 3D structural blurring. Instead, we propose multi-resolution supervision through wavelet transforms, progressively increasing resolution while preserving structural integrity:

$$\mathbf{C}_l = \mathcal{W}(\mathbf{C}, l) \quad (11)$$

where \mathbf{C} is ground truth color images, \mathcal{W} represents wavelet transform and l denotes the level of transformation. This approach avoids the zigzag artifacts of direct image rescaling, ensuring stable detail refinement during training. It enables the Gaussian model to first capture a rough scene representation with fewer Gaussians and later refine scene details for a more precise Gaussian distribution. Therefore, the photometric regularization is $\mathcal{L}_p = 0.8 * |\mathbf{C}_l - \bar{\mathbf{C}}| + 0.2 * SSIM(\mathbf{C}_l, \bar{\mathbf{C}})$.

Objective Function. During training, we jointly optimize explicit Gaussians and implicit SDF. We apply distortion \mathcal{L}_d and depth-normal \mathcal{L}_n regularization as defined in GOF [48]. The overall objective function is defined as:

$$\mathcal{L} = \mathcal{L}_p + \mathcal{L}_{geo} + \mathcal{L}_{sdf} + \lambda_d \mathcal{L}_d + \lambda_n \mathcal{L}_n. \quad (12)$$

Pruning. In our framework, where opacity is intrinsically linked to spatial position through the SDF relationship, we implement a geometry-aware pruning strategy that removes Gaussians exceeding the truncation threshold: $\bar{s}_i > tr$. This approach replaces conventional opacity-based pruning with a physically-grounded criterion that better aligns with our surface-aware representation.

Mesh Extraction. Previous Marching Cubes-based approaches [24, 45] must densely search both occupied and free space, leading to inefficiencies and resolution limitations, especially in unbounded scenes with coordinate distortions. In contrast, our method adapts Marching Tetrahedral [18] and exploits 3DGS’s spatial cues to constrain the search to regions only near Gaussians, avoiding unnecessary exploration of empty space while achieving superior surface alignment and reconstruction efficiency.

4. Experiments

4.1. Experimental Settings

Datasets. We comprehensively evaluate our method on three public datasets: *DTU* dataset [13] which consists of indoor object scans; *Tanks and Temples* [17] which features six unbounded outdoor scenes; and *Mip-NeRF* 360 [3] for measuring novel view synthesis quality.

Baselines. We compare our proposal against several state-of-the-art methods. Among implicit methods, we compare against NeRF [25], VolSDF [44], NeuS [37], N-angelo [21], GeoNeus [10], Instant NGP [27] and MipNeRF 360 [3]. As for explicit Gaussian methods, we compare against 3DGS [16], SuGaR [11], Mip-Splatting [47], 2DGS [12], GSurfel [8], 3DGSR [24], GS-Pull [55] and GOF [48].

Metrics. To evaluate our method, we follow common practice and report surface accuracy as Chamfer Distance and F1-score on DTU and Tanks and Temples, respectively. We measure the visual fidelity of the synthesized novel views with PSNR, SSIM and LPIPS [54] on Mip-NeRF 360.

Implementation. We perform single GPU training (NVIDIA 3090) and use by default $\lambda_d = 100$, $\lambda_n = 0.05$, $\lambda_{ns} = 1000$, $\lambda_{fs} = 10$, $\lambda_{depth} = 0.05$, $\lambda_{normal} = 0.1$ and $\beta = 100$. We train 30000 iterations like other methods and do not require extra training for SDF. For more implementation details, please refer to supp. mat..

4.2. Geometry Evaluation

We evaluate our method on the DTU dataset [13], comparing it with state-of-the-art surface reconstruction techniques. As shown in Table 1, our approach achieves the lowest Chamfer Distance, surpassing all existing 3DGS-based and implicit methods in both quality and efficiency. For N-angelo [21], we report results reproduced in [35], as the original values could not be verified. Figure 3 presents qualitative comparisons, where normal maps reveal that 2DGS [12] and GOF [48] often produce noisy, incomplete surfaces with artifacts, particularly struggling with flat regions. Our method mitigates these issues by constraining Gaussians to the surface via SDF, yielding smoother and more accurate reconstructions, especially in challenging areas with sparse camera coverage.

We then compare our method on the Tanks and Temples dataset [17]. The evaluation is focused exclusively on foreground objects, as the ground truth point cloud does not cover background regions. As shown in Table 2, our method achieves results on par with leading implicit approaches [21] while significantly reducing training time—optimizing large unbounded scenes in around 3 hours versus over 12 hours for implicit methods. Additionally, we slightly outperform GOF [48] while maintaining comparable rendering efficiency and faster mesh extraction (Table 4). Figure 4 showcases qualitative results, where our method excels at reconstructing flat surfaces, such as the Barn rooftop, and handling reflective and transparent windows in the Caterpillar and Truck scenes—areas where 2DGS [12] and GOF [48] struggle due to limited views and scene complexity. Our Gaussian-guided implicit surface reconstruction method ensures smooth and accurate reconstructions in these challenging scenarios.

	24	37	40	55	63	65	69	83	97	105	106	110	114	118	122	Mean
NeRF [25]	1.90	1.60	1.85	0.58	2.28	1.27	1.47	1.67	2.05	1.07	0.88	2.53	1.06	1.15	0.96	1.49
VolSDF [44]	1.14	1.26	0.81	0.49	1.25	0.70	0.72	1.29	1.18	0.70	0.66	1.08	0.42	0.61	0.55	0.86
NeuS [37]	1.00	1.37	0.93	0.43	1.10	0.65	0.57	1.48	1.09	0.83	0.52	1.20	0.35	0.49	0.54	0.84
N-angelo [21]	0.49	1.05	0.95	0.38	1.22	1.10	2.16	1.68	1.78	0.93	0.44	1.46	0.41	1.13	0.97	1.07
SuGaR [11]	1.47	1.33	1.13	0.61	2.25	1.71	1.15	1.63	1.62	1.07	0.79	2.45	0.98	0.88	0.79	1.33
2DGS [12]	0.48	0.91	0.39	0.39	1.01	0.83	0.81	1.36	1.27	0.76	0.70	1.40	0.40	0.76	0.52	0.80
GSurfel [8]	0.66	0.93	0.52	0.41	1.06	1.14	0.85	1.29	1.53	0.79	0.82	1.58	0.45	0.66	0.53	0.88
3DGSR [24]	0.68	0.84	0.70	0.39	1.16	0.87	0.77	1.48	1.26	0.87	0.69	0.80	0.42	0.64	0.60	0.81
GS-Pull [55]	0.51	0.56	0.46	0.39	0.82	0.67	0.85	1.37	1.25	0.73	0.54	1.39	0.35	0.88	0.42	0.75
GOF [48]	0.50	0.82	0.37	0.37	1.12	0.74	0.73	1.18	1.29	0.68	0.77	0.90	0.42	0.66	0.49	0.74
Ours	0.45	0.65	0.36	0.36	0.94	0.70	0.67	1.27	0.99	0.63	0.49	0.84	0.39	0.53	0.47	0.65

Table 1. **Quantitative Comparison on the DTU Dataset [13]**. We show the Chamfer distance. Our method achieves the highest reconstruction accuracy among all methods. For N-angelo [21], we report the results from UniSDF [35] reproduction and we show the vanilla results in supp. mat..



Figure 3. **Surface Reconstruction on the DTU Dataset [1]**. We show normal maps rendered from the reconstructed meshes. 2DGS [12] produces overly smooth surfaces with floating artifacts and outliers, while GOF [48] struggles to reconstruct flat surface. In contrast, our method generates smooth yet detailed surfaces without floating artifacts, demonstrating its superior ability to represent geometry accurately.

	Implicit			Explicit			
	NeuS [37]	GeoNeus [10]	N-angelo [21]	SuGaR [11]	2DGS [12]	GOF [48]	Ours
Barn	0.29	0.33	0.70	0.14	0.36	0.51	0.56
Caterpillar	0.29	0.26	0.36	0.16	0.23	0.41	0.38
Courthouse	0.17	0.12	0.28	0.08	0.13	0.28	0.29
Ignatius	0.83	0.72	0.89	0.33	0.44	0.68	0.72
Meetingroom	0.24	0.20	0.32	0.15	0.16	0.28	0.25
Truck	0.45	0.45	0.48	0.26	0.26	0.59	0.62
Average	0.38	0.35	0.50	0.19	0.30	0.46	0.47

Table 2. **Quantitative Results on the Tanks and Temples Dataset [17]**. Reconstructions are evaluated with the official evaluation scripts and we report F1-score. Our method outperforms all 3DGS-based surface reconstruction methods and performs comparably with the SOTA neural implicit methods while optimizing significantly faster.

4.3. Novel View Synthesis

We further compare our method with state-of-the-art novel view synthesis (NVS) methods on the Mip-NeRF 360 dataset [3]. Quantitative results in Table 3 indicate that our approach surpasses GOF [48] across all metrics in indoor scenes, while for outdoor scenes, the performance gap remains relatively small. However, our method significantly improves surface reconstruction quality. This suggests that our enhanced geometry representation leads to higher visual quality. Figure 5 presents a qualitative comparison of the extracted meshes. Consistent with our observations on the Tanks and Temples dataset [17], our method reconstructs

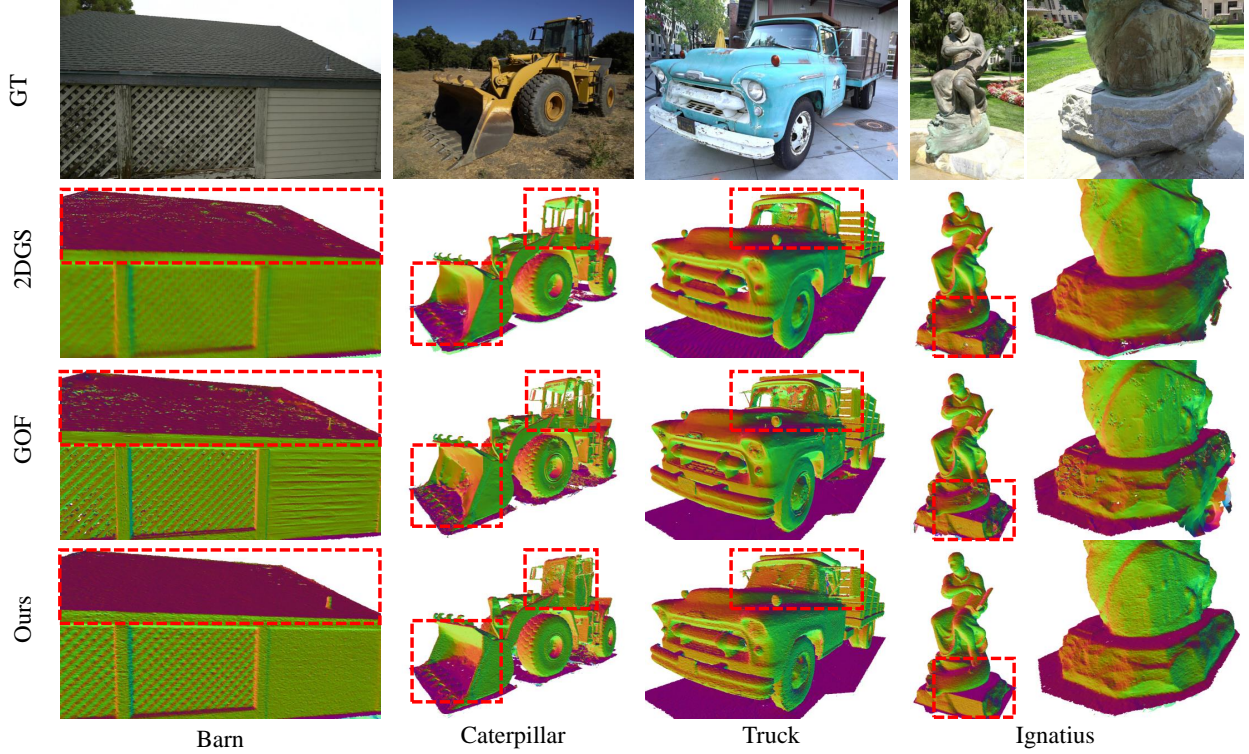


Figure 4. **Surface Reconstruction on the Tanks and Temples Dataset [17].** We show the rendered normal maps from reconstructed meshes. Results of 2DGS [12] and GOF [48] struggles to reconstruct smooth surfaces around transparent windows and produces noisy results in regions with sparse views. In contrast, our approach effectively handles transparent areas and achieves smooth reconstruction even in sparsely viewed regions.

	Outdoor Scene			Indoor Scene		
	PSNR \uparrow	SSIM \uparrow	LPIPS \downarrow	PSNR \uparrow	SSIM \uparrow	LPIPS \downarrow
NeRF [25]	21.46	0.458	0.515	26.84	0.790	0.370
Instant NGP [27]	22.90	0.566	0.371	29.15	0.880	0.216
MipNeRF360 [3]	24.47	0.691	0.283	31.72	0.917	0.180
3DGS [16]	24.64	0.731	0.234	30.41	0.920	0.189
SuGaR [11]	22.93	0.629	0.356	29.43	0.906	0.225
Mip-Splatting [47]	24.65	0.729	0.245	30.90	0.921	0.194
2DGS [12]	24.21	0.709	0.276	30.10	0.913	0.211
GS-Pull [55]	23.76	0.703	0.278	30.78	0.925	0.182
GOF [48]	24.82	0.750	0.202	30.79	0.924	0.184
Ours	24.78	0.743	0.211	30.83	0.930	0.166

Table 3. **Quantitative Results on Mip-NeRF 360 [3] Dataset.** Our method achieves comparable NVS results, especially in the indoor scenes in terms of LPIPS.

smooth, detailed meshes. In contrast, 2DGS [12] yields overly smooth meshes, and GOF [48] produces noisy artifacts on flat surfaces.

4.4. Ablation Study

4.4.1. Runtime Analysis

Table 4 presents a comprehensive runtime analysis on the Barn scene, highlighting our method’s efficiency and adaptability. Notably, our framework seamlessly integrates with existing Gaussian rasterizers, as demonstrated by the “Ours

Run Time	2DGS	Ours (2D)	GOF	Ours
Training	17 min	39 min	2.8 h	3.1 h
Meshing	~20 min	5 min	~30 min	5 min

Table 4. **Runtime.** We report the training and meshing time.

(2D)” implementation combining our approach with the 2DGS rasterizer. While the incorporation of SDF guidance enables superior surface reconstruction quality, our method maintains competitive training times comparable to efficient baselines like 2DGS and GOF. Furthermore, our approach achieves substantial acceleration in mesh extraction compared to existing methods.

4.4.2. Ablations on Different Regularizations

Ablations on SDF Fields. Table 5 quantitatively validates the effectiveness of our Gaussian-based implicit surface reconstruction framework compare with GOF. To further demonstrate the generalizability of our approach, we additionally evaluate its performance when integrated with the 2DGS rasterizer denoted as “Ours (2D)”, reporting consistent F1-score improvements across different configurations.

Ablations on Geometry Regularization. The ablation studies in Table 5 demonstrate the impact of different geometry regularization terms. Since the pseudo normal map is derived from the pseudo depth map, they exhibit identi-

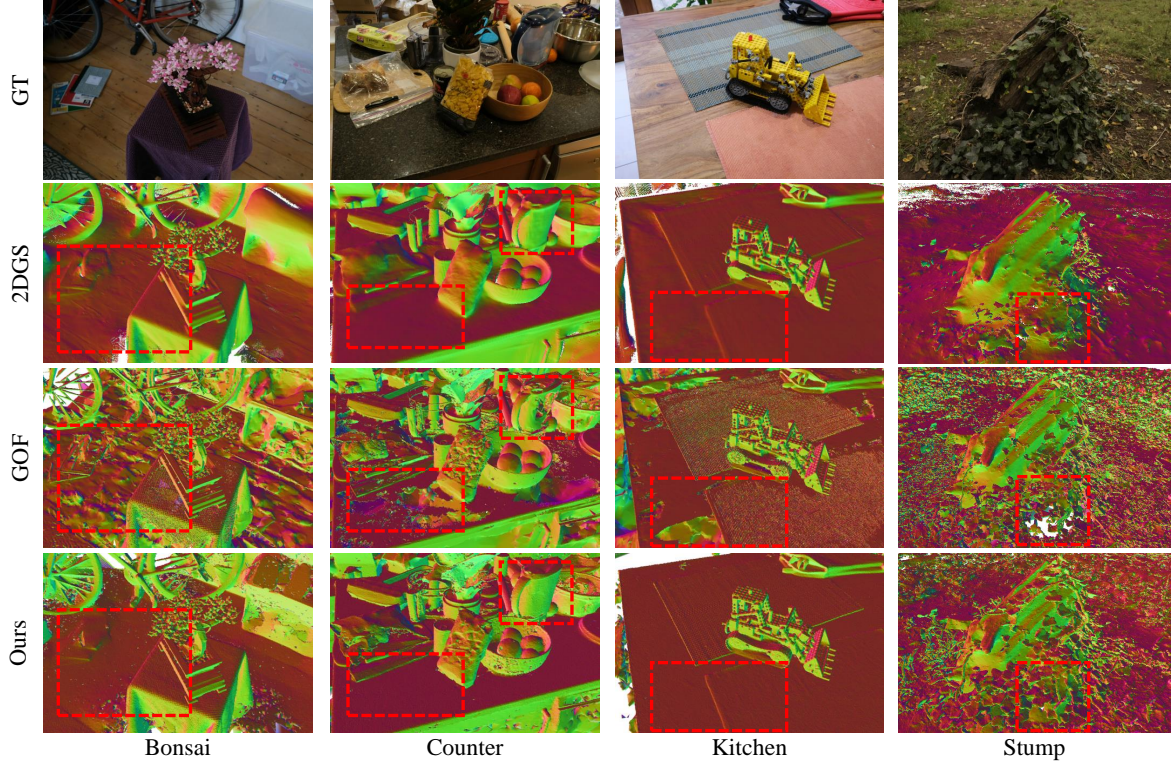


Figure 5. **Surface Reconstruction on the Mip-NeRF 360 Dataset [3].** We show the rendered normal maps from reconstructed meshes. GOF’s [48] meshes are noisy and fail to reconstruct smooth surface where there are reflection and curvature surface. In contrast, our method can generate smoother and detailed surface without any outlier points.

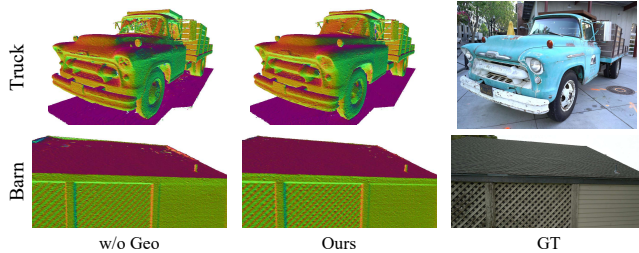


Figure 6. **Ablation Study on Geometry Regularization.**

Method	2DGS	Ours (2D)	$\lambda_D = 0$	$\lambda_N = 0$	$\lambda_D = 0, \lambda_N = 0$
F1 Score	0.36	0.40	0.52	0.51	0.50
Method	GOF	GOF+Geo	$\lambda_D = 0.5$	$\lambda_N = 0.5$	Ours
F1 Score	0.51	0.52	0.45	0.47	0.56

Table 5. **Quantitative Ablation Study.** We report F1 score of scene Barn with and without proposed regularization. We denote our method with default 3D Gaussian rasterizer [48] as “Ours” and with 2D Gaussian rasterizer [12] as “Ours (2D)”. “GOF+Geo” represents GOF with geometry cues only.

cal performance gaps. We further evaluate GOF enhanced with our geometry cues, denoted as “GOF+Geo”, which shows modest improvements (0.52). Due to the scale ambiguity problem, we set small values for λ_D, λ_N specifically (0.05 and 0.1 for Tanks and Temples, 0.01 and 0.01

for DTU and MipNeRF 360). We demonstrate that increasing these weights to 0.5 actually degrades the results by introducing adverse effects from geometric cues. We also demonstrate the error distribution after alignment in supp. mat., showcasing the limitation of geometry cues. The most significant enhancement is achieved through our complete pipeline (8% improvement), highlighting the synergistic effect of our integrated approach. Figure 6 demonstrates the effectiveness of our geometry regularization in handling transparent and flat regions, significantly improving reconstruction quality through enhanced surface consistency.

5. Conclusion

We introduce MonoGSDF, a Gaussian-based implicit surface reconstruction framework. Our SDF-to-Opacity function bridges implicit and explicit representations, while Gaussian-guided normalization ensures stable optimization across unbounded 3D scenes. A multi-resolution training strategy, enhanced by the geometric cues, progressively refines reconstruction quality. Our method achieves state-of-the-art accuracy and efficiency, effectively handling complex cases such as flat and transparent surfaces where existing approaches often struggle.

References

[1] Henrik Aanæs, Rasmus Ramsbøl Jensen, George Vogiatzis, Engin Tola, and Anders BJORHOLM Dahl. Large-scale data for multiple-view stereopsis. *International Journal of Computer Vision*, pages 1–16, 2016. 6

[2] Xu Baixin, Hu Jiangbei, Li Jiaze, and He Ying. Gsurf: 3d reconstruction via signed distance fields with direct gaussian supervision. *arXiv preprint arXiv:2411.15723*, 2024. 2

[3] Jonathan T Barron, Ben Mildenhall, Dor Verbin, Pratul P Srinivasan, and Peter Hedman. Mip-nerf 360: Unbounded anti-aliased neural radiance fields. In *Proceedings of the IEEE/CVF conference on computer vision and pattern recognition*, pages 5470–5479, 2022. 2, 4, 5, 6, 7, 8, 1

[4] Danpeng Chen, Hai Li, Weicai Ye, Yifan Wang, Weijian Xie, Shangjin Zhai, Nan Wang, Haomin Liu, Hujun Bao, and Guofeng Zhang. Pgss: Planar-based gaussian splatting for efficient and high-fidelity surface reconstruction. *arXiv preprint arXiv:2406.06521*, 2024. 2

[5] Hanlin Chen, Fangyin Wei, Chen Li, Tianxin Huang, Yunsong Wang, and Gim Hee Lee. Vcr-gaus: View consistent depth-normal regularizer for gaussian surface reconstruction. *arXiv preprint arXiv:2406.05774*, 2024. 2

[6] Yiwen Chen, Zilong Chen, Chi Zhang, Feng Wang, Xiaofeng Yang, Yikai Wang, Zhongang Cai, Lei Yang, Huaping Liu, and Guosheng Lin. Gaussianeditor: Swift and controllable 3d editing with gaussian splatting. In *Proceedings of the IEEE/CVF Conference on Computer Vision and Pattern Recognition*, pages 21476–21485, 2024. 1

[7] Brian Curless and Marc Levoy. A volumetric method for building complex models from range images. In *Proceedings of the 23rd annual conference on Computer graphics and interactive techniques*, pages 303–312, 1996. 1

[8] Pinxuan Dai, Jiamin Xu, Wenxiang Xie, Xinguo Liu, Huamin Wang, and Weiwei Xu. High-quality surface reconstruction using gaussian surfels. In *ACM SIGGRAPH 2024 Conference Papers*, pages 1–11, 2024. 2, 5, 6

[9] Zhiwen Fan, Wenyan Cong, Kairun Wen, Kevin Wang, Jian Zhang, Xinghao Ding, Danfei Xu, Boris Ivanovic, Marco Pavone, Georgios Pavlakos, et al. Instantssplat: Unbounded sparse-view pose-free gaussian splatting in 40 seconds. *arXiv preprint arXiv:2403.20309*, 2, 2024. 2

[10] Qiancheng Fu, Qingshan Xu, Yew Soon Ong, and Wenbing Tao. Geo-neus: Geometry-consistent neural implicit surfaces learning for multi-view reconstruction. *Advances in Neural Information Processing Systems*, 35:3403–3416, 2022. 5, 6

[11] Antoine Guédon and Vincent Lepetit. Sugar: Surface-aligned gaussian splatting for efficient 3d mesh reconstruction and high-quality mesh rendering. In *Proceedings of the IEEE/CVF Conference on Computer Vision and Pattern Recognition*, pages 5354–5363, 2024. 1, 2, 5, 6, 7

[12] Binbin Huang, Zehao Yu, Anpei Chen, Andreas Geiger, and Shenghua Gao. 2d gaussian splatting for geometrically accurate radiance fields. In *ACM SIGGRAPH 2024 Conference Papers*, pages 1–11, 2024. 1, 2, 3, 5, 6, 7, 8

[13] Rasmus Jensen, Anders Dahl, George Vogiatzis, Engil Tola, and Henrik Aanæs. Large scale multi-view stereopsis evaluation. In *2014 IEEE Conference on Computer Vision and Pattern Recognition*, pages 406–413. IEEE, 2014. 5, 6, 1, 4

[14] Michael Kazhdan, Matthew Bolitho, and Hugues Hoppe. Poisson surface reconstruction. In *Proceedings of the fourth Eurographics symposium on Geometry processing*, 2006. 1

[15] Nikhil Keetha, Jay Karhade, Krishna Murthy Jatavallabhula, Gengshan Yang, Sebastian Scherer, Deva Ramanan, and Jonathon Luiten. Splatam: Splat track & map 3d gaussians for dense rgb-d slam. In *Proceedings of the IEEE/CVF Conference on Computer Vision and Pattern Recognition*, pages 21357–21366, 2024. 1

[16] Bernhard Kerbl, Georgios Kopanas, Thomas Leimkühler, and George Drettakis. 3d gaussian splatting for real-time radiance field rendering. *ACM Trans. Graph.*, 42(4):139–1, 2023. 1, 2, 3, 5, 7

[17] Arno Knapitsch, Jaesik Park, Qian-Yi Zhou, and Vladlen Koltun. Tanks and temples: Benchmarking large-scale scene reconstruction. *ACM Transactions on Graphics (ToG)*, 36(4):1–13, 2017. 5, 6, 7

[18] Jonas Kulhanek and Torsten Sattler. Tetra-nerf: Representing neural radiance fields using tetrahedra. In *Proceedings of the IEEE/CVF International Conference on Computer Vision*, pages 18458–18469, 2023. 2, 5

[19] Jiahe Li, Jiawei Zhang, Xiao Bai, Jin Zheng, Xin Ning, Jun Zhou, and Lin Gu. Dngaussian: Optimizing sparse-view 3d gaussian radiance fields with global-local depth normalization. In *Proceedings of the IEEE/CVF Conference on Computer Vision and Pattern Recognition*, pages 20775–20785, 2024. 2

[20] Yanyan Li, Chenyu Lyu, Yan Di, Guangyao Zhai, Gim Hee Lee, and Federico Tombari. Geogaussian: Geometry-aware gaussian splatting for scene rendering. In *European Conference on Computer Vision*, pages 441–457. Springer, 2025. 2

[21] Zhaoshuo Li, Thomas Müller, Alex Evans, Russell H Taylor, Mathias Unberath, Ming-Yu Liu, and Chen-Hsuan Lin. Neuralangelo: High-fidelity neural surface reconstruction. In *Proceedings of the IEEE/CVF Conference on Computer Vision and Pattern Recognition*, pages 8456–8465, 2023. 5, 6, 1, 4

[22] Tianqi Liu, Guangcong Wang, Shoukang Hu, Liao Shen, Xinyi Ye, Yuhang Zang, Zhiguo Cao, Wei Li, and Ziwei Liu. Mvsgaussian: Fast generalizable gaussian splatting reconstruction from multi-view stereo. In *European Conference on Computer Vision*, pages 37–53. Springer, 2025. 2

[23] Tao Lu, Mulin Yu, Linning Xu, Yuanbo Xiangli, Limin Wang, Dahua Lin, and Bo Dai. Scaffold-gs: Structured 3d gaussians for view-adaptive rendering. In *Proceedings of the IEEE/CVF Conference on Computer Vision and Pattern Recognition*, pages 20654–20664, 2024. 2, 3

[24] Xiaoyang Lyu, Yang-Tian Sun, Yi-Hua Huang, Xiuzhe Wu, Ziyi Yang, Yilun Chen, Jiangmiao Pang, and Xiaojuan Qi. 3dgsr: Implicit surface reconstruction with 3d gaussian splatting. *arXiv preprint arXiv:2404.00409*, 2024. 1, 2, 3, 4, 5, 6

[25] Ben Mildenhall, Pratul P Srinivasan, Matthew Tancik, Jonathan T Barron, Ravi Ramamoorthi, and Ren Ng. Nerf:

Representing scenes as neural radiance fields for view synthesis. *Communications of the ACM*, 65(1):99–106, 2021. 2, 5, 6, 7

[26] Thomas Müller, Brian McWilliams, Fabrice Roussel, Markus Gross, and Jan Novák. Neural importance sampling. *ACM Transactions on Graphics (ToG)*, 38(5):1–19, 2019. 3

[27] Thomas Müller, Alex Evans, Christoph Schied, and Alexander Keller. Instant neural graphics primitives with a multiresolution hash encoding. *ACM Trans. Graph.*, 41(4):102:1–102:15, 2022. 5, 7

[28] Thomas Müller, Alex Evans, Christoph Schied, and Alexander Keller. Instant neural graphics primitives with a multiresolution hash encoding. *ACM transactions on graphics (TOG)*, 41(4):1–15, 2022. 2, 3

[29] Michael Niemeyer, Fabian Manhardt, Marie-Julie Rakotosaona, Michael Oechsle, Daniel Duckworth, Rama Gosula, Keisuke Tateno, John Bates, Dominik Kaeser, and Federico Tombari. Radsplat: Radiance field-informed gaussian splatting for robust real-time rendering with 900+ fps. *arXiv preprint arXiv:2403.13806*, 2024. 2

[30] Zhiyin Qian, Shaofei Wang, Marko Mihajlovic, Andreas Geiger, and Siyu Tang. 3dgs-avatar: Animatable avatars via deformable 3d gaussian splatting. In *Proceedings of the IEEE/CVF Conference on Computer Vision and Pattern Recognition*, pages 5020–5030, 2024. 1

[31] Xiaowei Song, Jv Zheng, Shiran Yuan, Huan-ang Gao, Jingwei Zhao, Xiang He, Weihao Gu, and Hao Zhao. Sags: Scale-adaptive gaussian splatting for training-free anti-aliasing. *arXiv preprint arXiv:2403.19615*, 2024. 2

[32] Cheng Sun, Min Sun, and Hwann-Tzong Chen. Direct voxel grid optimization: Super-fast convergence for radiance fields reconstruction. In *Proceedings of the IEEE/CVF conference on computer vision and pattern recognition*, pages 5459–5469, 2022. 2

[33] Jiaxiang Tang, Jiawei Ren, Hang Zhou, Ziwei Liu, and Gang Zeng. Dreamgaussian: Generative gaussian splatting for efficient 3d content creation. *arXiv preprint arXiv:2309.16653*, 2023. 1

[34] Matias Turkulainen, Xuqian Ren, Iaroslav Melekhov, Otto Seiskari, Esa Rahtu, and Juho Kannala. Dn-splatter: Depth and normal priors for gaussian splatting and meshing. *arXiv preprint arXiv:2403.17822*, 2024. 1, 2, 4, 3

[35] Fangjinhua Wang, Marie-Julie Rakotosaona, Michael Niemeyer, Richard Szeliski, Marc Pollefeys, and Federico Tombari. Unisdf: Unifying neural representations for high-fidelity 3d reconstruction of complex scenes with reflections. *arXiv preprint arXiv:2312.13285*, 2023. 5, 6, 4

[36] Junjie Wang, Jiemin Fang, Xiaopeng Zhang, Lingxi Xie, and Qi Tian. Gaussianeditor: Editing 3d gaussians delicately with text instructions. In *Proceedings of the IEEE/CVF Conference on Computer Vision and Pattern Recognition*, pages 20902–20911, 2024. 1

[37] Peng Wang, Lingjie Liu, Yuan Liu, Christian Theobalt, Taku Komura, and Wenping Wang. Neus: Learning neural implicit surfaces by volume rendering for multi-view reconstruction. *arXiv preprint arXiv:2106.10689*, 2021. 5, 6

[38] Shuzhe Wang, Vincent Leroy, Yohann Cabon, Boris Chidlovskii, and Jerome Revaud. Dust3r: Geometric 3d vision made easy. In *Proceedings of the IEEE/CVF Conference on Computer Vision and Pattern Recognition*, pages 20697–20709, 2024. 2

[39] Yaniv Wolf, Amit Bracha, and Ron Kimmel. Surface reconstruction from gaussian splatting via novel stereo views. *arXiv preprint arXiv:2404.01810*, 2024. 2

[40] Zhiwen Yan, Weng Fei Low, Yu Chen, and Gim Hee Lee. Multi-scale 3d gaussian splatting for anti-aliased rendering. In *Proceedings of the IEEE/CVF Conference on Computer Vision and Pattern Recognition*, pages 20923–20931, 2024. 2

[41] Lihe Yang, Bingyi Kang, Zilong Huang, Zhen Zhao, Xiaogang Xu, Jia Shi Feng, and Hengshuang Zhao. Depth anything v2. *arXiv preprint arXiv:2406.09414*, 2024. 4

[42] Runyi Yang, Zhenxin Zhu, Zhou Jiang, Baijun Ye, Xiaoxue Chen, Yifei Zhang, Yuantao Chen, Jian Zhao, and Hao Zhao. Spectrally pruned gaussian fields with neural compensation. *arXiv preprint arXiv:2405.00676*, 2024. 2

[43] Ziyi Yang, Xinyu Gao, Wen Zhou, Shaohui Jiao, Yuqing Zhang, and Xiaogang Jin. Deformable 3d gaussians for high-fidelity monocular dynamic scene reconstruction. In *Proceedings of the IEEE/CVF Conference on Computer Vision and Pattern Recognition*, pages 20331–20341, 2024. 1

[44] Lior Yariv, Jiatao Gu, Yoni Kasten, and Yaron Lipman. Volume rendering of neural implicit surfaces. *Advances in Neural Information Processing Systems*, 34:4805–4815, 2021. 5, 6

[45] Mulin Yu, Tao Lu, Lining Xu, Lihan Jiang, Yuanbo Xiangli, and Bo Dai. Gsdf: 3dgs meets sdf for improved rendering and reconstruction. *arXiv preprint arXiv:2403.16964*, 2024. 1, 2, 4, 5

[46] Zehao Yu, Songyou Peng, Michael Niemeyer, Torsten Sattler, and Andreas Geiger. Monosdf: Exploring monocular geometric cues for neural implicit surface reconstruction. *Advances in neural information processing systems*, 35:25018–25032, 2022. 4

[47] Zehao Yu, Anpei Chen, Binbin Huang, Torsten Sattler, and Andreas Geiger. Mip-splatting: Alias-free 3d gaussian splatting. In *Proceedings of the IEEE/CVF Conference on Computer Vision and Pattern Recognition*, pages 19447–19456, 2024. 2, 5, 7

[48] Zehao Yu, Torsten Sattler, and Andreas Geiger. Gaussian opacity fields: Efficient adaptive surface reconstruction in unbounded scenes. *ACM Transactions on Graphics*, 2024. 1, 2, 5, 6, 7, 8

[49] Ye Yuan, Xueteng Li, Yangyi Huang, Shalini De Mello, Koki Nagano, Jan Kautz, and Umar Iqbal. Gavatar: Animatable 3d gaussian avatars with implicit mesh learning. In *Proceedings of the IEEE/CVF Conference on Computer Vision and Pattern Recognition*, pages 896–905, 2024. 1

[50] Vladimir Yugay, Yue Li, Theo Gevers, and Martin R Oswald. Gaussian-slam: Photo-realistic dense slam with gaussian splatting. *arXiv preprint arXiv:2312.10070*, 2023. 1

[51] Baowen Zhang, Chuan Fang, Rakesh Shrestha, Yixun Liang, Xiaoxiao Long, and Ping Tan. Rade-gs: Rasterizing depth in

gaussian splatting. *arXiv preprint arXiv:2406.01467*, 2024.

[2](#)

[52] Jiahui Zhang, Fangneng Zhan, Muyu Xu, Shijian Lu, and Eric Xing. Fregs: 3d gaussian splatting with progressive frequency regularization. In *Proceedings of the IEEE/CVF Conference on Computer Vision and Pattern Recognition*, pages 21424–21433, 2024. [5](#)

[53] Kai Zhang, Gernot Riegler, Noah Snavely, and Vladlen Koltun. Nerf++: Analyzing and improving neural radiance fields. *arXiv preprint arXiv:2010.07492*, 2020. [2](#)

[54] Richard Zhang, Phillip Isola, Alexei A Efros, Eli Shechtman, and Oliver Wang. The unreasonable effectiveness of deep features as a perceptual metric. In *Proceedings of the IEEE conference on computer vision and pattern recognition*, pages 586–595, 2018. [5](#)

[55] Wenyuan Zhang, Yu-Shen Liu, and Zhizhong Han. Neural signed distance function inference through splatting 3d gaussians pulled on zero-level set. *Advances in Neural Information Processing Systems*, 37:101856–101879, 2025. [1](#), [2](#), [5](#), [6](#), [7](#)

[56] Xiaoyu Zhou, Zhiwei Lin, Xiaojun Shan, Yongtao Wang, Deqing Sun, and Ming-Hsuan Yang. Drivinggaussian: Composite gaussian splatting for surrounding dynamic autonomous driving scenes. In *Proceedings of the IEEE/CVF Conference on Computer Vision and Pattern Recognition*, pages 21634–21643, 2024. [1](#)

[57] Matthias Zwicker, Hanspeter Pfister, Jeroen Van Baar, and Markus Gross. Ewa splatting. *IEEE Transactions on Visualization and Computer Graphics*, 8(3):223–238, 2002. [3](#)

MonoGSDF: Exploring Monocular Geometric Cues for Gaussian Splatting-Guided Implicit Surface Reconstruction

Supplementary Material

A. Implementation Details

A.1. Hyperparameters

In the following, we report implementation details and hyperparameters used for our method.

Gaussian Splatting. For hyperparameters used in the Gaussian rasterization, we follow previous works [12, 16, 48]. We train our Gaussian model and SDF network jointly with 30000 iterations. We set the initial learning rate for Gaussians' position as 0.00016 and the final initial learning rate as 0.0000016. And we set learning rates for scales and rotation as 0.005, 0.001, respectively. We start the Gaussian densification after 500 iterations and until 15000 iterations. We densify Gaussians every 100 iterations and the gradient threshold for densification is 0.0002. We start the distortion loss \mathcal{L}_d and the depth-normal loss \mathcal{L}_n after 3000 iterations and 7000 iterations, respectively. And we set the wavelet level as 3 and gradually increase the resolution until 10000 iteration. After that, we use the full resolution for training.

SDF Network. We use two-layer MLPs and the hidden dimension is 32. We initialize β from Eq. 5 as 100. We start train our SDF from 5000 iterations and until 30000 iterations. The learning rate for our SDF network is 0.002. For each iteration, we sample $M = 10000$ pixels and $K_n = 11$, $K_f = 64$ points.

Geometry Regularization. We set the learning rate for s, t, a, b in Eq. 7 as 0.01. And for Tanks and Temples, we set $\lambda_D = 0.05$, $\lambda_N = 0.1$, for DTU and Mip-NeRF 360, we set $\lambda_D = 0.01$, $\lambda_N = 0.01$.

B. Distortion and Depth-Normal Loss

We apply a distortion loss [12] and depth-normal loss [48] as discussed in Section 3.2. The distortion loss concentrates the weight distribution along the rays by minimizing the distance between the ray-splat intersections:

$$\mathcal{L}_d = \sum_{i,j} \omega_i \omega_j |z_i - z_j|, \quad (13)$$

where $\omega_i = o_i(x) \prod_{j=1}^{i-1} (1 - o_j(x))$ is the blending weight of the i -th intersection and z_i is the depth of the intersection points. The depth-normal loss is defined as:

$$\mathcal{L}_n = \sum (1 - \bar{\mathbf{N}} \cdot \nabla(\bar{D})), \quad (14)$$

where $\nabla(\bar{D})$ is the gradient of rendered Gaussian Depth.

C. Additional Experimental Results

C.1. Results on DTU and Mip-NeRF 360

In Table 7, we present the results reported in the Neuralangelo publication [21] on the DTU dataset. It is important to note that the quantitative results from the Neuralangelo paper have been flagged by other studies and discussions on the official GitHub repository as non-reproducible[†].

To provide a more comprehensive evaluation, we include additional qualitative comparisons on the DTU dataset [13] in Figure 13 and further demonstrate results on the Mip-NeRF 360 dataset [3] in Figure 14. Our method excels in handling reflective surfaces and produces reconstructions that are not only smoother but also exhibit finer details, highlighting its capability for more accurate and visually appealing scene representations.

D. More Ablation

D.1. Ablation on Different Rasterizers

In Figure 7, we present reconstruction results using different Gaussian rasterizers, showcasing the versatility and adaptability of our method. These results demonstrate that our approach can be seamlessly integrated into existing Gaussian methods, no matter it's 2D Gaussians [12] or 3D Gaussians [48], enhancing their performance without requiring significant modifications. Furthermore, our method consistently delivers high-quality reconstructions with fine details, highlighting its effectiveness in capturing intricate scene structures such as transparent and reflection areas.

D.2. Ablations on Normalization Function.

We acknowledge that non-uniform transformation like Mip-NeRF's [3] non-linear normalization (mapping $\pm\infty$ to $(-2, 2)$) can cause distortions and conflicts with tiny-cudann's requirements of having inputs in $(0, 1)$. In contrast, our method applies a near-linear transformation for Gaussians within the initial bounding box and a compression for outliers, minimizing distortion effects. As shown in Table 6, our approach ("Ours") outperforms MipNeRF's normalization function ("w/ MipNeRF NF") which is also scaled to $(0, 1)$.

D.3. Ablations on SDF to Opacity Function.

We compare results using 3DGSR's [24] SDF-to-Opacity function (denoted as "w/ 3DGSR SDF2O" in Table 6) with

[†]Refer to this [GitHub issue](#) for details.

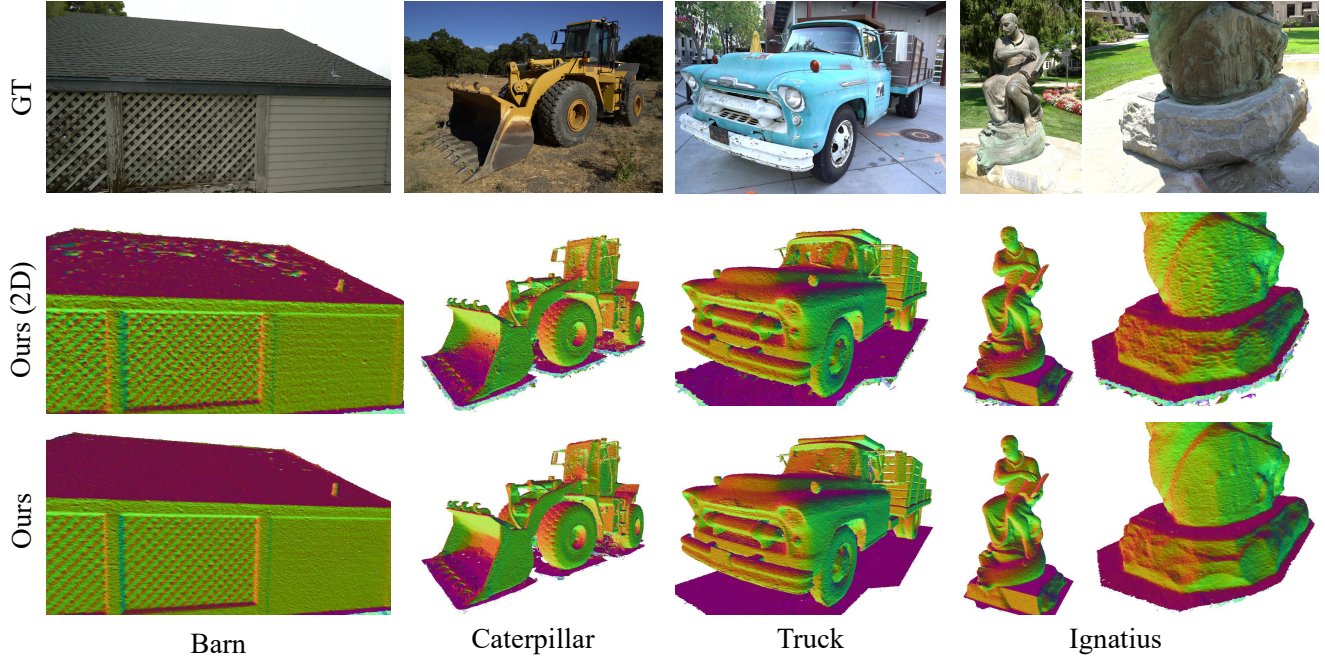


Figure 7. Mesh Extraction with Different Gaussian Rasterizer.

Method	w/ MipNeRF NF	w/ 3DGSR SDF2O	Ours
F-score	0.52	0.24	0.56

Table 6. **Ablation Study on Normalization and SDF to Opacity.**
We show the F-score of reconstructed mesh on Barn.

our proposed function (Eq. 5). Our method achieves a higher f-score, offering a simpler, more efficient solution and the ability to reach full opacity of 1, unlike 3DGSR’s capped opacity of 0.25. While 3DGSR targets object-level reconstruction, this limitation may impede its effectiveness in unbounded outdoor scenes.

D.4. Ablations on Geometry Cues.

Our analysis reveals significant artifacts in Depth Anything v2’s estimated depth maps due to inherent scale uncertainty, despite global alignment attempts. As shown in Figure 8, we compare our alignment method “Ours” with DN Splatter’s approach [34] “DN Align”, demonstrating our method’s superior ability to reduce depth errors between rendered and aligned pseudo depth. Interestingly, despite the inaccuracies in DN Splatter’s aligned pseudo depth, the reconstruction F1 score remains comparable to our method. This finding suggests that while these limitations underscore the unreliability of pseudo depth maps for precise reconstruction, necessitating our model’s strong ability to compensate for misalignments, the primary improvement stems from our novel Gaussian-SDF collaboration pipeline rather than geometric cues alone.

D.5. Ablations on Pruning Strategy.

Our method links the opacity value of each Gaussian to its SDF value with our SDF-to-Opacity function. While this maintains computational equivalence to conventional opacity-based pruning, it provides a physically-grounded criterion.

D.6. Ablations on Multi-Resolution Regularization.

Our Multi-Resolution training strategy employs a coarse-to-fine approach, initially utilizing fewer Gaussians at lower resolutions to establish robust scene geometry before progressively refining details. Figure 10 quantitatively illustrates the controlled growth of Gaussian populations throughout training. While the quantitative results remain the same since the evaluation only focus on foreground objects, the qualitative results shows significant improvement. Figure 9 demonstrates the effectiveness of our approach, showing that multi-resolution regularization enables reliable reconstruction of objects with limited views, whereas standard training struggles in such scenarios.

D.7. Ablations on Different Meshing Methods.

Figure 11 illustrates the limitations of depth fusion-based mesh extraction in unbounded scenes, revealing significant distortion caused by resolution constraints and Mip-NeRF’s [3] normalization artifacts. Comparative results in Figure 12 demonstrate our method’s advantages across different meshing techniques, showing that our Gaussian-

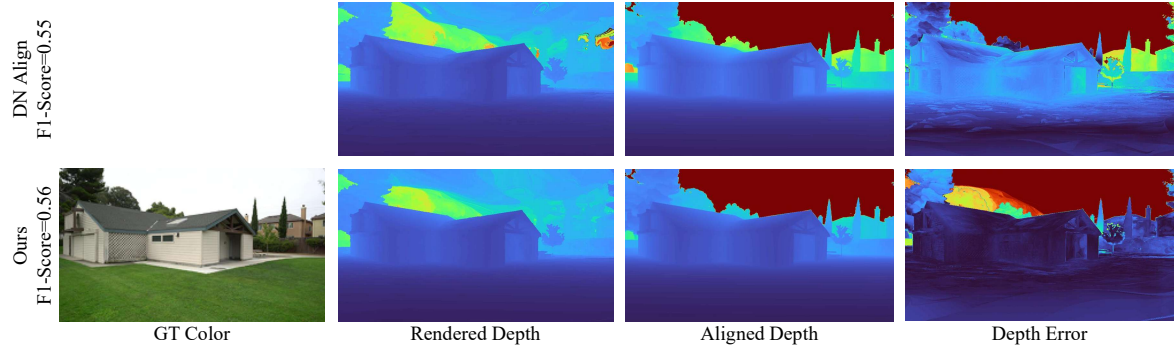


Figure 8. **Ablations on Geometry Cues.** We show the ground truth color image, rendered depth, aligned pseudo depth and depth error (in log) on Barn. DN Align represents our pipeline with DN Splatter’s [34] alignment.

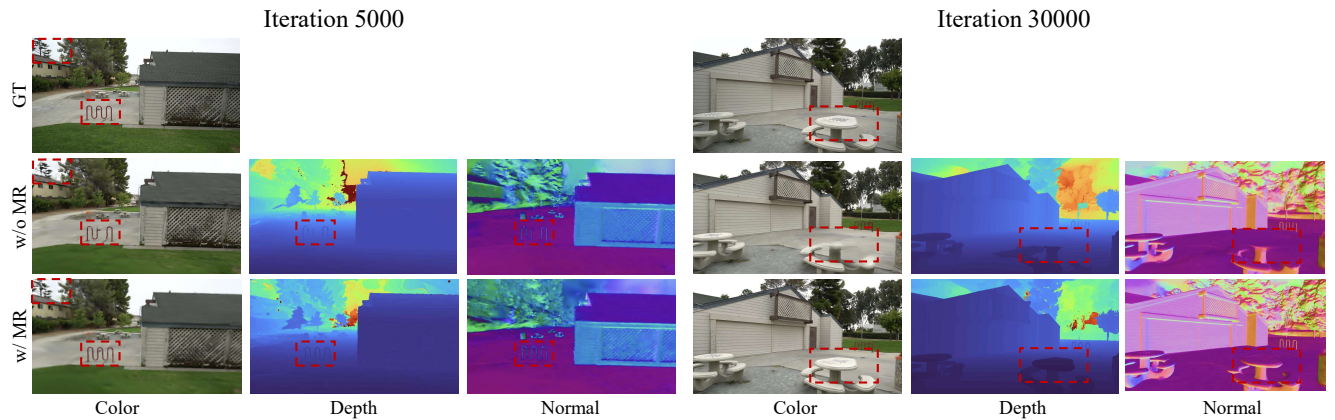


Figure 9. **Ablation Study on Multi-Resolution Regularization.** We show a comparison of ground truth color images alongside our rendered color, depth, and normal outputs at various training iterations on Barn. The results demonstrate that our multi-resolution regularization enables more efficient and complete scene geometry reconstruction, achieving superior convergence compared to standard training approaches.

guided surface reconstruction achieves both superior efficiency and enhanced detail preservation compared to existing approaches.

E. Limitation Discussion

The pseudo depth maps exhibit high uncertainty in the far distance regions and inconsistency across multiple views, which limits our method’s ability to reconstruct distant background areas, such as the sky. However, since foreground objects are the primary focus in reconstruction tasks, our method demonstrates superior performance in these regions. To address this limitation, we plan to introduce an uncertainty-based weighting mechanism for the geometry regularization.

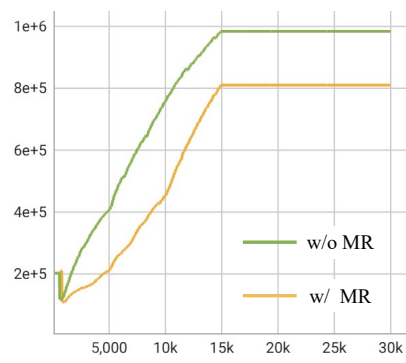


Figure 10. **Total Gaussian Population Growth on Barn (Training Iterations vs. Gaussian Count).** Our proposed multi-resolution regularization achieves comparable reconstruction and rendering quality with significantly fewer Gaussians than standard training approaches, demonstrating improved computational efficiency without compromising output quality.

	24	37	40	55	63	65	69	83	97	105	106	110	114	118	122	Mean
N-angelo [21]	0.49	1.05	0.95	0.38	1.22	1.10	2.16	1.68	1.78	0.93	0.44	1.46	0.41	1.13	0.97	1.07
N-angelo* [21]	0.37	0.72	0.35	0.35	0.87	0.54	0.53	1.29	0.97	0.73	0.47	0.74	0.32	0.41	0.43	0.61
Ours	0.45	0.65	0.36	0.36	0.94	0.70	0.67	1.27	0.99	0.63	0.49	0.84	0.39	0.53	0.47	0.65

Table 7. **Quantitative Comparison on the DTU Dataset [13].** We show the Chamfer distance. For Neuralangelo [21], we report the results from UniSDF [35] reproduction as N-angelo, and the results from Neuralangelo publication as N-angelo*, which is not reproducible.

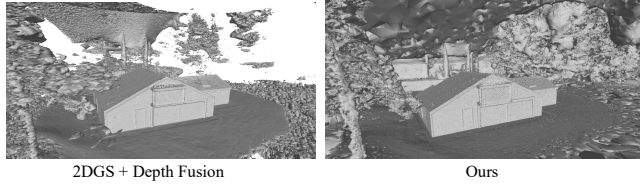


Figure 11. **Comparison on Depth Fusion and Ours on Barn.**

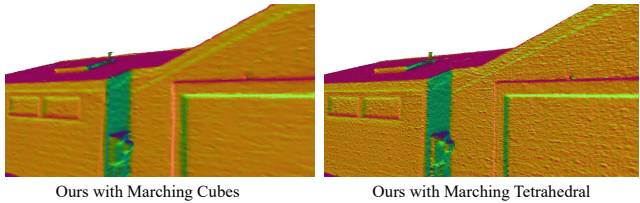


Figure 12. **Ablation Study on Different Meshing Methods.** While Marching Cubes struggles with resolution limitations in unbounded scene reconstruction, resulting in low-quality meshes with missing details, our method consistently produces high-quality meshes with enhanced geometric fidelity and preserved fine structures.

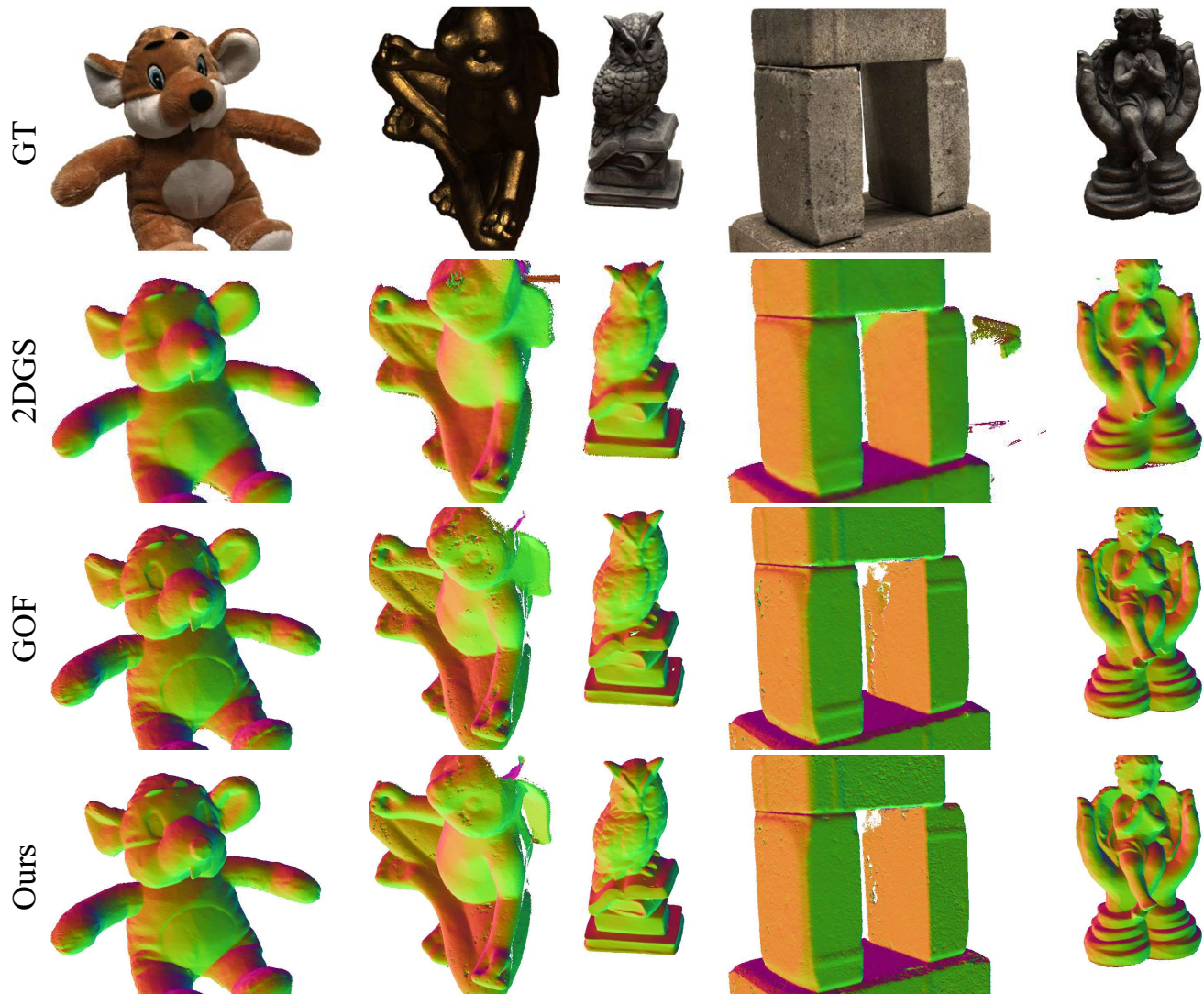


Figure 13. Additional Results on DTU [13].

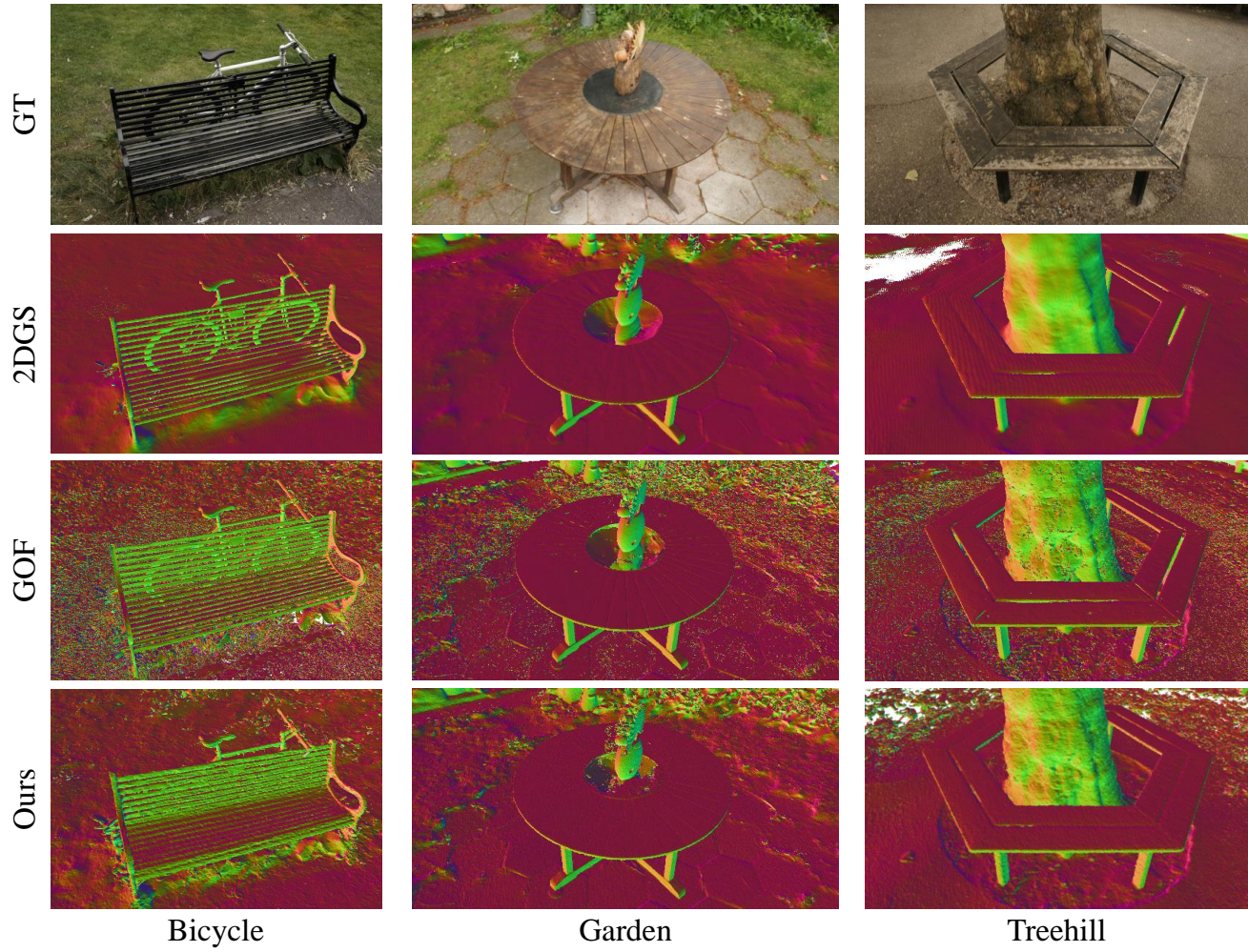


Figure 14. Additional Results on Mip-NeRF 360 [3].